

# Energy-selective X-ray CT imaging with an EIGER2 hybrid photon counting detector in a Diondo d<sub>2</sub> XCT system

Jorge Martinez-Garcia<sup>1</sup>, Damian Gwerder<sup>1</sup>, David Schiffmann<sup>1</sup>, Thomas Thuering<sup>2</sup>, Dubravka Šišak Jung<sup>2</sup>,  
Spyridon Gkoumas<sup>2</sup>, Philipp Schuetz<sup>1</sup>

<sup>1</sup>Lucerne University of Applied Sciences and Arts, School for Engineering and Architecture, Competence Center for Thermal Energy Storage, Horw, CH, e-mail: {jorge.martinezgarcia, damian.gwerder01, philipp.schuetz} @hslu.ch

<sup>2</sup>DECTRIS Ltd, Täfernweg 1, 5405, Baden, CH, e-mail: {thomas.thuering, dubravka.sisak, spyridon.gkoumas} @dectris.com

## Abstract

Hybrid photon counting (HPC) detector having high spatial resolution and photon energy discrimination capabilities can remarkably improve the quality of X-ray computed tomography (XCT) measurements. In this contribution, we report on the integration of an HPC (EIGER2) detector in a Diondo d<sub>2</sub> XCT system and present imaging results for two different samples. It is shown that the detector performs well in the Diondo d<sub>2</sub> XCT system allowing to resolve components of different densities in all examined samples. A higher quality of the images was achieved for lower energy threshold values. The integration of the HPC detector required remarkable data postprocessing on the acquired projections as described here. The approach described here enables the exploitation of energy-selective XCT imaging.

**Keywords:** X-ray, hybrid photon counting, computed tomography, data postprocessing, energy-selective imaging

## 1 Introduction

Industrial X-ray computed tomography (XCT) is a non-destructive key technology to image the internal three-dimensional (3D) structure of material samples at micron resolutions. While the technique is promising for internal inspections, the quality of the acquired XCT images is a critical factor for reliable assessments, and particularly, when further quantitative data processing is the subject of interest [1]. In addition to the settings of the X-ray source (e.g., acceleration voltage, tube current and filtration), the image quality is also remarkably impacted by the detection hardware. Nowadays, modern industrial cone-beam XCT systems are typically equipped with flat-panel energy-integrating X-ray (EI) detectors based on a scintillator material to convert the impinging X-ray photons into visible light. The generated visible light is then converted into electrical signals by photodiodes and integrated over time for the complete time frame of the image acquisition [2]. Such technology provides high spatial resolution combined with fast image acquisition rates. However, it measures the energy integrated signals of all detected X-ray photons only, thus skipping all the energy dependent information (e.g., one photon of 60 keV could produce the same signal as three photons of 20 keV, whereas their transmission through the object is quite different). On the other hand, images acquired with EI detectors are unavoidably affected by beam hardening artefacts [3].

In contrast, hybrid photon-counting (HPC) detector technology is based on direct conversion of X-ray photons into electric charge cloud (from electron-hole pairs) generating a voltage pulse proportional to the photon's energy. In this technology, application-specific integrated circuits (ASICs) connected at each detector element allows to classify the signals according to their energy values (i.e., height of the pulse) and thus discriminate between different photon's energy reaching the detector by comparing them with a suitable set of adjustable energy thresholds [4]. This energy discriminating capability of HPC detectors results in multiple advantages when scanning multicomponent materials: (i) elimination of beam hardening artefacts, (ii) increasing the image contrast of low absorbing components by giving more weights to low energy photons, (iii) elimination of electronic noise and (iv) to perform material differentiation from a single acquisition using the wide-spectrum, thus, avoiding the need of repeated XCT scans with different (filtered) polychromatic spectra [5,6]. While the benefits of HPC technology are significant, the performance of current HPC detectors is also somewhat limited by physical effects, such as charge sharing, K-escape and pulse pileup [7].

HPC detectors have found successful applications in the fields of low energy-electron microscopy [8], advanced X-ray diffraction [4,9] and medical X-ray imaging [7,10-12]. In this contribution, we report on the integration of an



HPC (EIGER2) detector in an industrial Diondo d<sub>2</sub> XCT system from Diondo, Hattingen, Germany and provide first results of imaging of different samples.

## 2 Materials and Methods

The samples analysed in this work were a vertebral disk and a sample of concentric rings composed of different materials. High-resolution XCT measurements were performed on a commercial Diondo d<sub>2</sub> XCT device from Diondo, Hattingen, Germany, equipped with an X-ray source (XWT-225 TCHE+), from X-RAY worX GmbH, Garbsen, Germany. An EIGER2 CdTe 2M-W HPC detector from DECTRIS Ltd, Switzerland, was used in the measurements. The detector is built from four modules with an active area of 311.1 mm x 38.4 mm (4148 pixels x 512 pixels) and has maximum count rate capability of  $1 \times 10^8$  photons/s/mm<sup>2</sup>. It is equipped with a cadmium-telluride (CdTe) sensor with the added benefit of high spatial resolution due to its pixel size of 75  $\mu$ m and provides an adjustable energy threshold range from 4 to 80 keV with two energy thresholds. The data acquisition and preprocessing approach adopted in this work is described in the following. The collected 3D imaging data was reconstructed with the X-AID software from MITOS using the Feldkamp-Davis-Kreiss algorithm.



Figure 1: Internal view of the Diondo d<sub>2</sub> X-CT cabine showing the EIGER2 CdTe 2M-W HPC detector from DECTRIS (a) positioned between the X-ray source XWT-225 TCH+ from X-RAY worX (b) and the EI detector 4343DX-I fromVarex (c), during a CT image acquisition. The vertical adjustable stand (d) allows for switchable use between the HPC and EI detectors.

### 2.1 Data acquisition

During the data acquisition the HPC EIGER2 detector was positioned and properly aligned inside the XCT cabine on top of a vertical adjustable stand in-between the X-ray source XWT-225 TCH+ from X-RAY worX and the standard EI detector 4343DX-I from Varex Salt Lake City, U.S.A, as illustrated in Figure 1. As the control software of Diondo2 is not open, the EIGER detector was not integrated in the control software. To coordinate sample rotation with EIGER image acquisition, a modified version of the acquisition software was used where a new sample position was set whenever a new image acquisition of the EIGER detector was completed. As the scanning software required also the Varex detector to record images, this was set on the highest pixel binning mode (16 x 16) to store only small images and framebinning 1 to enable a fast reaction of the system (as the system wait on the Varex detector). The EIGER's parameters were set directly into the Python-based acquisition packages accessing the detector through the HTTP-based RESTlike API provided by DECTRIS, as documented in the SIMPLON API [13]. An acquisition time

of about 1300 ms was set for the measurements. This value fairly exceeds the integration time provided by the Varex detector in the binning mode ( $\sim 90$  ms), ensuring that Varex acquisition is completed once the EIGER acquisition is done. The scans were performed in such a way that for each sample position (during the rotation),  $N$  projections were collected for each defined threshold. Prior to that both flat and dark field images were collected for subsequent flat field pixel correction as discussed in the following.

## 2.2 Flat-field correction

X-ray sources are far from being uniform and detectors show pixel-to-pixel variations in sensitivity that significantly degradate the image quality. To correct those systematic errors due to dark current, beam inhomogeneity and potential imperfections in the detector, flat-field correction (FFC) of the collected projection images is required [14,15]. The conventional FFC method requires to acquire projection images without sample with and without the X-ray beam turned on, which are referred to as flat fields and dark fields, respectively. The dark-field images ( $D$ ), account for the dark current of the detector causing the detector pixels to report values different from zero, even when no X-ray photons are hitting it (Fig. 2d). The flat-field images ( $F$ ), on the other hand, account for the inhomogeneities of the X-ray beam showing how “unflat” the X-ray imaging system is (Fig. 2e). Based on the acquired flat and dark fields, the measured projection images with sample ( $P$ ) are then normalised to new images ( $P'$ ) as:

$$P' = \frac{(P-D)}{(F-D)} \quad (1)$$

In this work four  $P$  and four  $D$  images were collected with EIGER2 and their corresponding averaged images were introduced in Eq.1 for FFC. An example of the procedure's output for one of the samples examined in this work is shown in Figure 2 and discussed in Section 3.

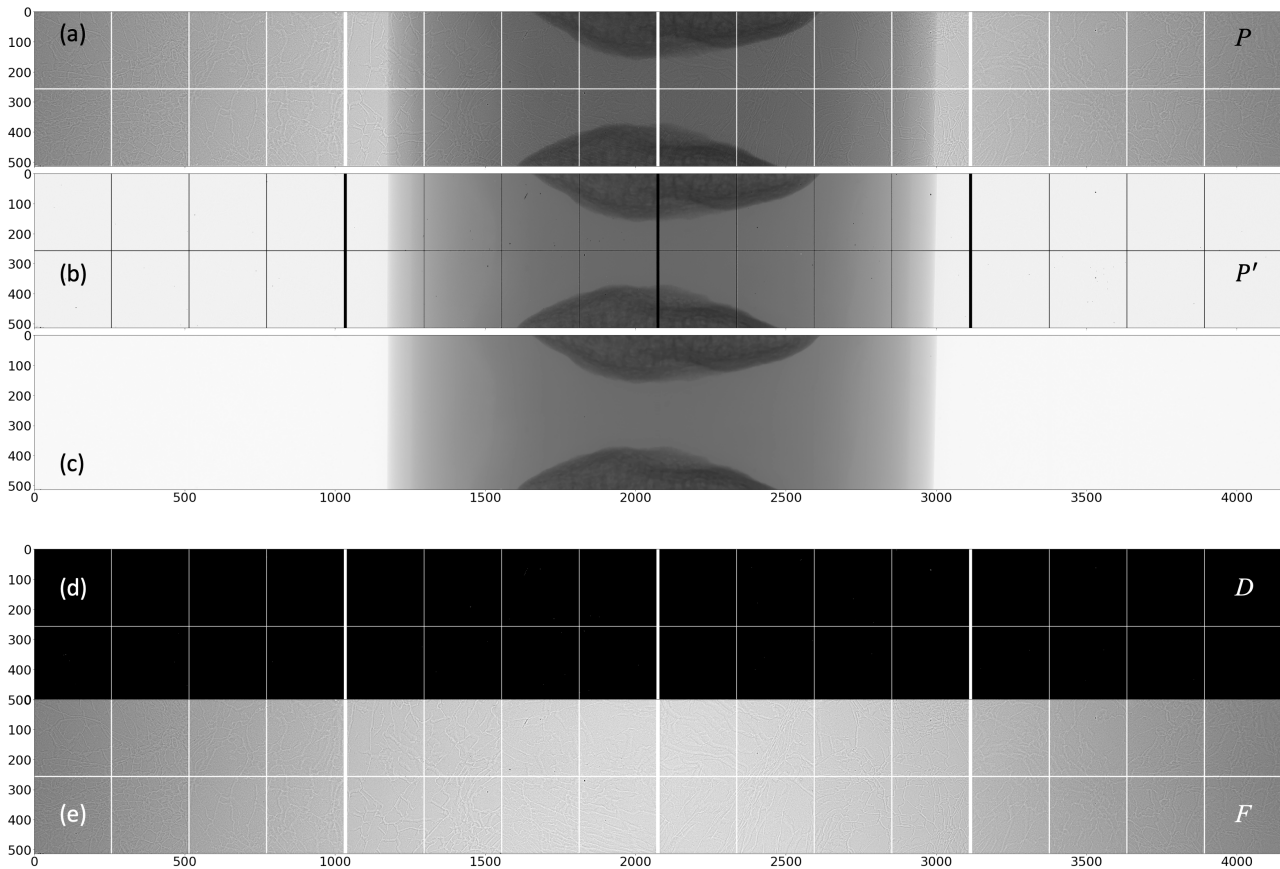
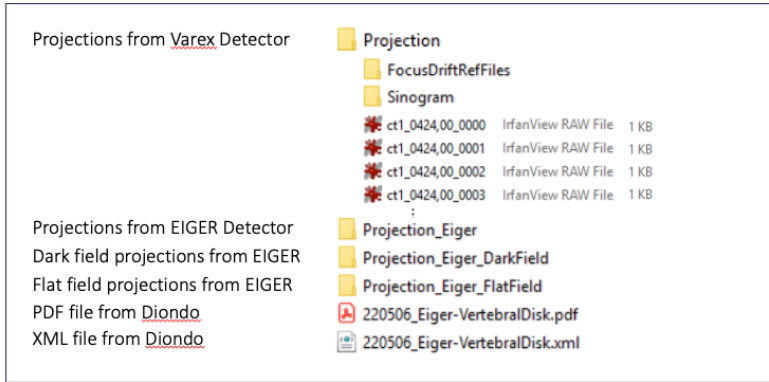


Figure 2: Measured projection images with the EIGER2 detector. Projection images collected for a vertebral disk are illustrated before (a) and after applying flat-field correction (b). (c) Same projection image as (b) after applying bad-pixel correction. (d) Detector output (dark field image) collected with the X-ray source switched off. (e) Detector output (flat-field image) when irradiated by the X-ray beam without sample.

## 2.3 Postprocessing data workflow

To reconstruct 3D imaging data from the projection images measured with the EIGER detector, the standard output data structure produced by the Diondo's software is required as initial step. Relevant data files were then processed to generate a similar final data output structure updated with the EIGER's measurements. To accomplish this, a set of Python scripts were written to: (i) automatically set the right EIGER's parameters into the XML file required for the X-AID software for data reconstruction, (ii) properly correct the projections acquired with EIGER and (iii) re-allocated the data files as described in Figure 3.

### I Initial data output



### II Data processing

1. Delete projections from Varex (RAWs files)
2. Modify XML file from Diondo with Eiger's parameters
3. Split up projections from EIGER into different folders for each examined threshold
4. Apply flat-field and bad-pixel corrections to the EIGER's projections
5. Re-allocate the corrected EIGER-projections into the Diondo-projection folder for subsequent data reconstruction

### III Final data output

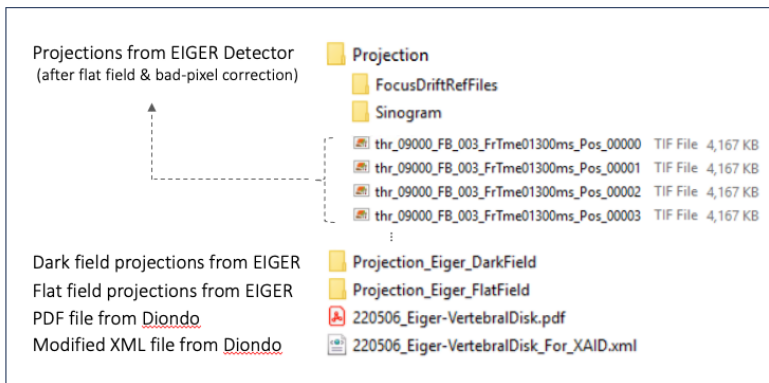


Figure 3: Schematic of the post-processing data workflow before image reconstruction. The standard output data structure from the Diondo's software is taken as starting point (I). Data files output from EIGER and Varex measurements are modified and re-allocated according to a sequence of steps (II). An updated data output structure is generated for data reconstruction (III).

## 3 Results and discussion

Figure 2 shows a projection of one the sample examined before and after FFC respectively. As it can be seen from the figure, the FFC approach successfully reduces intensity inhomogeneities in the collected projections  $P$ . However, it fails in removing properly the response from “dead” pixels allocated along the gap-lines between the detector elements (dark vertical and horizontal lines in Fig. 2a-b) and defective (“bad”) pixels appearing randomly on the active area of the detector. As those pixels behave the same whether or not they are illuminated, they were identified from the measured dark and flat fields as those at which,  $F - D = 0$ . Once identified, their values were replaced in the output image by linearly interpolated values derived from the nearby neighbouring pixels' output in combination with a 3x3 median filter mask, as illustrated in Figure 2c.

Reconstruction of the 3D volume from the collected 2D projection images was carried with the X-AID software [16]. To account for potential motion of the sample during the CT acquisition and small misalignment of the detector, Linear Drift and Centershift corrections were performed prior the reconstruction using the functionality of the software. Optimisation of the slant angle (i.e., the angle of detector tilt around the axis lying on the detector plane along its horizontal direction) was also required to achieve optimal results.



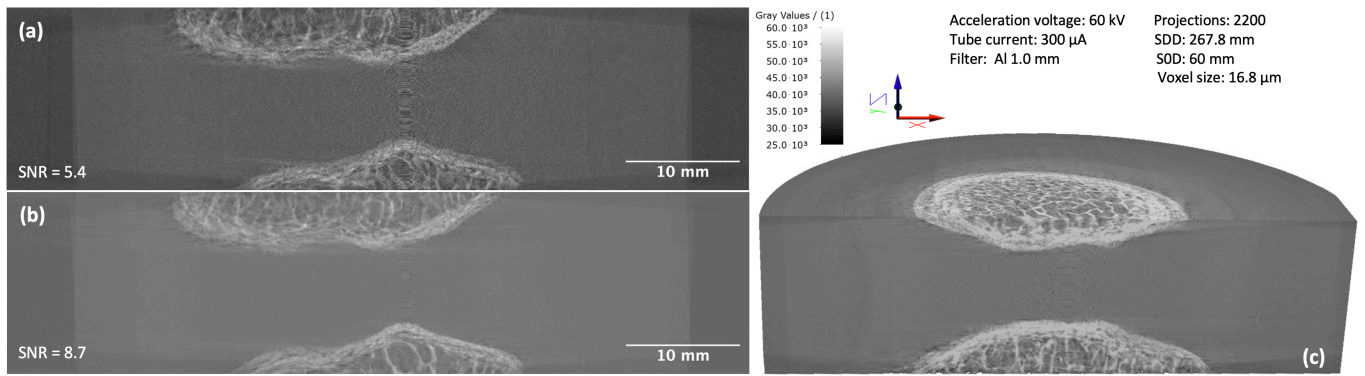


Figure 4: Imaging results and XCT parameters for the vertebral disk sample. a) Cross-section of the XCT data obtained with an energy threshold of 43 keV: only X-ray photons with energy higher than 43 keV are counted. b) Same as in (a) but with 9 keV threshold. (c) 3D rendering of the XCT images obtained with 9 keV energy threshold.

Figure 4 shows the results obtained for the examined vertebral-disk sample together with the used XCT parameters. Clearly a good contrast between bone (brighter region) and surrounding tissues was achieved. In this case study, the use of lower values of the X-ray tube acceleration voltages (e.g. 60 kV), or equivalently low energy photons, allows for a greater contrast. As it can be also seen, a substantially noise reduction is achieved when switching the energy threshold parameter from 43 keV (Fig. 1a) to 9 keV (Fig. 1b), as witnessed by an increase in signal to noise ratio (SNR) of 61.1%. This is because the lower the energy threshold value is the higher the number of photons counted by the detector thus allowing better statistics.

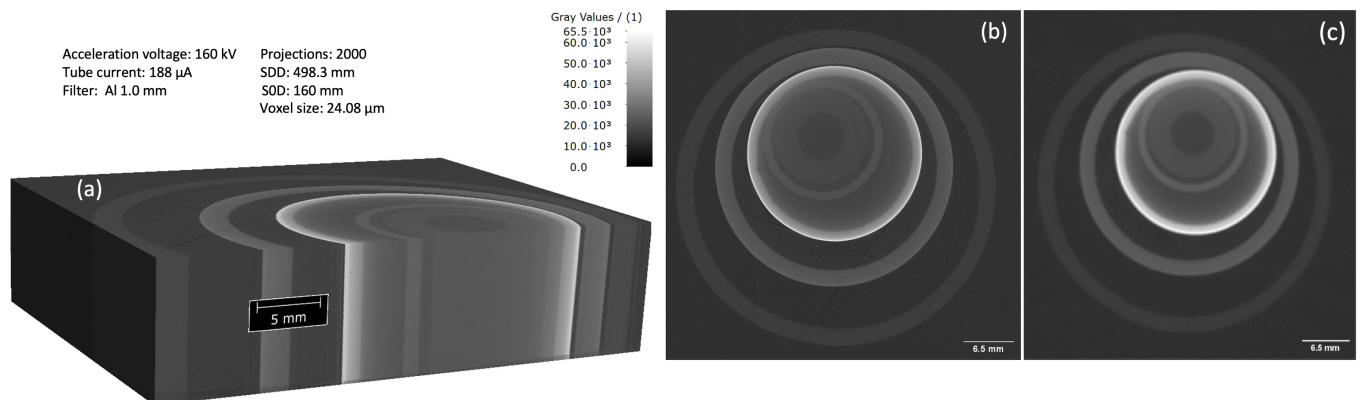


Figure 5: Imaging results and XCT parameters for the concentric ring sample. Each individual ring is made of plastic, aluminium, and steel. a) 3D rendering of the XCT images. b) Cross-section of the XCT data obtained with the EIGER2 detector c) Similar cross-section as shown in a) but derived from the XCT scan data collected with the Varex EI 4343DX-I detector.

Figure 5 displays the imaging results and the corresponding XCT parameters used in the acquisition for the concentric ring sample. Each individual ring is made of plastic, aluminium, and steel. As it can be seen, material components of different densities can be resolved very well, based on the high contrast achieved. It can also be seen that the HPC EIGER2 detector is more effective by resolving the edges and reducing beam hardening artefacts (Fig. 2b) than the standard EI detector from Varex (Fig. 2c). However, the EIGER2 performance is not flawless, as multiple ring artefacts were present and partially corrected during the 3D volume reconstruction.

## 4 Conclusions

The integration of an HPC (EIGER2) detector in an industrial Diondo d<sub>2</sub> XCT system has been reported and first results of imaging two different samples have been presented. It has been shown that the use of lower threshold energy values allows for better contrast and noise reduction. Comparison between EIGER2 and the EI detector

revealed that EIGER2 resulted more effective in resolving edges and reducing beam hardening artefacts for one of the examined samples.

## Acknowledgements

The authors would like to thank to the Swiss National Science Foundation, Switzerland for the support of the acquisition of the LuCi instrument (Grant 206021-189608) and the support of the research projects CutAWAY, Switzerland (Grant 200021E-183684) and Investigation of Salt Hydrates Segregation with XCT, Switzerland (Grant 200021-201088).

## References

- [1] S. Carmignato, W. Dewulf, R. Leach, Industrial X-Ray Computed Tomography, Springer Cham 2018.
- [2] T. M. Buzug, Computed tomography: from photon statistics to modern cone-beam CT, Springer Berlin, 2008.
- [3] D. Panetta, Advances in X-ray detectors for clinical and preclinical Computed Tomography, Nucl. Instrum. Methods Phys. Res. A 809 (2016), 2-12.
- [4] T. Donath, D. Sisak Jung, M. Burian et al., EIGER2 hybrid-photon-counting detectors for advanced synchrotron diffraction experiments, J. Synchrotron Rad. 30 (2023), 723-738.
- [5] J. Fornaro, S. Leschka, D. Hibbeln, A. Butler, N. Anderson et al., Dual- and multi-energy CT: approach to functional imaging, Insights Imaging, 2 (2011), 149-159.
- [6] Thorsten R. C. Johnson, Dual-Energy CT: General Principles, Am. J. Roentgenol, 199(5) (2012), S3-8.
- [7] K. Taguchi and J. S. Iwanczyk, Vision 20/20: Single photon counting x-ray detectors in medical imaging, Med. Phys. 40 (2013), 100901.
- [8] G. Tinti et al., The EIGER detector for low-energy electron microscopy and photoemission electron microscopy, J. Synchrotron Rad. 24 (2017), 963-974.
- [9] G. B. M. Vaughan et al., ID15A at the ESRF - a beamline for high-speed operando X-ray diffraction, diffraction tomography and total scattering, J. Synchrotron Rad. 27 (2020), 515-528.
- [10] J. Dudak, High-resolution X-ray imaging applications of hybrid-pixel photon counting detectors timepix, Radiat. Meas. 123 (2020). 106409.
- [11] J. Dudak, et al., Microtomography with photon counting detectors: improving the quality of tomographic reconstruction. by voxel-space oversampling, J. Inst. Met. 12 (2017), C01060.
- [12] Bjoern Kreisler, Photon counting detectors: Concept, technical challenges and clinical outlook, Eur. J. Radiol. 149 (2022) 110229.
- [13] [https://media.dectris.com/210607-DECTRIS-SIMPLON-API-Manual\\_EIGER2-chip-based\\_detectors.pdf](https://media.dectris.com/210607-DECTRIS-SIMPLON-API-Manual_EIGER2-chip-based_detectors.pdf)
- [14] J. Lifton and T. Liu, Ring artefact reduction via multi-point piecewise linear flat field correction for X-ray computed tomography, Optics Express 27 (2019), 3217-3228.
- [15] L. Tlustos et al., Signal variations in high-granularity Si pixel detectors, IEEE Trans Nucl Sci. 51 (2004), 3006-3012.
- [16] <https://x-aid.de>